Microsc. Microanal. 15, 441–453, 2009
doi:10.1017/S1431927609990389

Microscopy AND Microanalysis

© MICROSCOPY SOCIETY OF AMERICA 2009

Characterizing the Two- and Three-Dimensional Resolution of an Improved Aberration-Corrected STEM

A.R. Lupini,* A.Y. Borisevich, J.C. Idrobo, H.M. Christen, M. Biegalski, and S.J. Pennycook

Oak Ridge National Laboratory, 1 Bethel Valley Road, Oak Ridge, TN 37831, USA

Abstract: The successful development of third-order aberration correctors in transmission electron microscopy has seen aberration-corrected electron microscopes evolve from specialist projects, custom built at a small number of sites to common instruments in many modern laboratories. Here we describe some initial results illustrating the two- and three-dimensional (3D) performance of an aberration-corrected scanning transmission electron microscope with a prototype improved aberration corrector designed to also minimize fifth-order aberrations and a new, higher brightness gun. We show that atomic columns separated by 0.63 Å can be resolved and demonstrate detection of single dopant atoms with 3D sensitivity.

Key words: STEM, aberration, spherical, resolution, 3D

Introduction

Spherical aberration (C_3 or C_s) is well known in optics, where it was caused by the use of spherical lenses. This aberration is of particular relevance to electron microscopy because round electron lenses will always suffer from positive spherical aberration (Scherzer, 1936), and it sets the resolution limit in most modern transmission electron microscopes (TEMs). However, a little over 60 years ago, Scherzer set out how to overcome this aberration by breaking the rotational symmetry (Scherzer, 1947). As round electron lenses still offer a range of benefits, an aberration corrector is used to produce a negative spherical aberration to cancel the positive aberration of the round lenses. The key to implementing such a corrector is to obtain the desired negative spherical aberration while restoring rotational symmetry after the corrector.

There are two main classes of aberration corrector in use today. A quadrupole-octupole corrector uses quadrupoles to distort the beam and octupoles to correct the third-order aberrations (see Koops, 1978; Zach & Haider, 1995; Hawkes & Kasper, 1996; Dellby et al., 2001; Haider et al., 2008; Krivanek et al., 2008*a*). The hexapole (or equivalently "sextupole") style of corrector used for the present work has been described by several authors (Beck, 1979; Crewe & Kopf, 1980; Hawkes & Kasper, 1996) and in particular detail by Rose (1981, 1990, 2003). The action of a hexapole corrector is interesting because the leading order properties of a hexapole do not appear suitable to correct spherical aberration. However, any long multipole system will have higher order effects due to the propagation of the electrons along the axis. For a long hexapole these higher order effects include spherical aberration. A hexapole corrector must cancel out the leading effect due to the threefold symmetry, while retaining the desired negative spherical aberration. In such a corrector, round lenses provide an excellent way to transfer the image of each hexapole to the next, canceling the threefold astigmatism (C_{23} or A_2, depending on notation), and then to the objective lens. The round lenses also allow the magnification of the corrector, and so the amount of aberration correction, to be adjusted. Furthermore, they allow the effective optical separation to be varied, providing some control over higher order aberrations (Shao, 1988). The advantage of a hexapole corrector is that the off-axis and high-order aberrations can be small (Rose, 1990), while one disadvantage is that the alignment tolerance required is very precise. In all correctors very stable electronics are required (Haider et al., 2008). In practice, many of the key alignments are handled by software and so the user level operation is often remarkably similar for both types of corrector. Correction of aberrations up to and including the third-order spherical aberration has been demonstrated on both systems. However, the residual aberrations still provide an important limit to the resolution (Hartel et al., 2004). In this article we consider some initial results from the FEI Titan equipped with two different hexapole correctors: first, a conventional CEOS corrector "CESCOR," later replaced with an improved corrector "DCOR" designed to reduce the residual aberrations and a prototype high-brightness gun. Reviews of work from other aberration-corrected instruments can be found elsewhere (Rose, 2003; Varela et al., 2005; Lentzen, 2006; Lupini et al., 2007; Pennycook et al., 2008; Smith, 2008). Here we give a brief description of the instrument, characterize the resolu-

Received May 16, 2009; accepted June 26, 2009
**Corresponding author*. E-mail: 9az@ornl.gov

tion in first two and then three dimensions, and finally examine single atom detection with some three-dimensional (3D) sensitivity.

Materials and Methods

One way to consider image formation in the scanning transmission electron microscope (STEM) is to think of the presample optics as projecting an image of the electron source onto the sample, forming a probe. The effective size of this probe therefore is constrained by the source properties, limitations of the optics (geometrical aberrations, chromatic effects, and the diffraction limit), and instabilities. The probe is scanned over the sample and a signal is collected as a function of probe position to form an image. The high-angle scattering, which depends approximately on the square of the atomic number Z, is collected on a high-angle annular dark field detector to form a Z-contrast image. Other signals that can be acquired simultaneously include the electron energy loss spectrum (EELS) and the (also aberration-corrected) bright-field (BF) image.

The Titan S installed at Oak Ridge National Laboratory (ORNL) is based on the commercially available FEI Titan 80-300 scanning transmission electron microscope (STEM) and operates at 300 kV. This microscope was initially fitted with a standard Schottky field emission gun (FEG), FEI monochromator, and CEOS aberration corrector on the probe-forming side. During the course of the TEAM project (see http://ncem.lbl.gov/TEAM-project/index.html), the gun and the aberration corrector were upgraded to respectively improve the brightness and the higher order aberrations, and the monochromator was removed. The Ronchigram is observed directly on the viewing screen and presently the user has to remain in close proximity to the column. The FEI Titan 0.5 at Lawrence Berkeley National Laboratory, also developed as part of the TEAM project, has been demonstrated to have an information limit of just below 0.5 Å (Kisielowski et al., 2008). The Titan S at ORNL is a slightly earlier model with differences including a larger pole-piece gap, different suspension, and less acoustic isolation.

In a STEM the resolution will depend on the effective source size, and the signal-to-noise ratio will depend upon the amount of current in the probe. Source brightness is therefore important for a STEM because it will determine the amount of current available for a probe of a given size, and once emitted from the source, there is no practical way for brightness to be increased. Brightness B is commonly defined as the amount of current I per unit area (diameter d) per solid angle (half-angle α):

$$B = \frac{4I}{\pi^2 d^2 \alpha^2}. \tag{1}$$

It is also sometimes helpful to use the reduced brightness, which is obtained by dividing equation (1) by the relativistically corrected accelerating voltage. The condenser lenses are used to demagnify the image of the source so that it does not limit the probe. However, the trade-off is that spatial demagnification will magnify the angles, and because only a finite angular range is admitted to form the probe, this will reduce the current available. In practice, there will be a compromise between producing a smaller, more coherent probe and obtaining enough current to provide an analytically useful signal. The brightness of the source installed at ORNL was significantly improved by FEI and was measured as about 3×10^{13} A m^{-2} sr^{-1} at 300 kV ($\sim 0.8 \times 10^8$ A m^{-2} sr^{-1} V^{-1}) with an energy spread ΔE of about 0.8 eV. Remarkably, this brightness is almost the same as would be expected for a cold FEG ($\sim 1 \times 10^8$ A m^{-2} sr^{-1} V^{-1} from Krivanek et al., 2008*b*).

Having shown that the tip performance should be suitable for sub-Ångstrom resolution, the geometrical aberrations need to be considered. Figure 1 illustrates the phase shift due to typical aberration values measured for the two types of hexapole correctors. As the lower order aberrations are manually optimized by the user while looking at the image, defocus (C_1) and astigmatism (A_1) were manually set to zero. To illustrate usable aperture sizes, a 25 mrad aperture is marked for the CESCOR and 35 mrad for the DCOR. We repeated aberration measurements under a variety of conditions for both correctors. Typical values for the residual aberrations for both correctors are shown in Table 1. This table illustrates the importance of accurate measurement because the residual aberration values are very close to the uncertainty in the measurement.

It is these residual and higher order aberrations that limit the size of aperture and thus the resolution that can be achieved. Theoretical work has shown that adjusting the round lenses allows the fifth-order round aberration C_5 to be adjusted (Shao, 1988; Rose, 1990), which has been demonstrated experimentally (Hartel et al., 2004). We typically measured the C_5 of the CESCOR corrector as close to zero but saw values between about ± 4 mm. The measured values depended on the precise lens settings and sample height, but they probably mostly indicate the limited measurement accuracy. Calculations and further measurements reveal that there is an uncorrectable resolution limit due to the fifth-order sixfold astigmatism for the CESCOR. This aberration is C_{56} in the Nion style notation (Krivanek et al., 1999) and A_5 in the CEOS notation (Müller et al., 2006). We typically measured A_5 as about 1–3 mm, which agrees reasonably well with the expected value (Müller et al., 2006), and note that high-order aberrations are hard to measure accurately. These values reveal that the nonround fifth-order aberrations are significant in the CESCOR design, although they compare favorably to the fifth-order aberrations of the second generation QO corrector that are typically around 50–100 mm. In practice, we found that it was possible to resolve spacings down

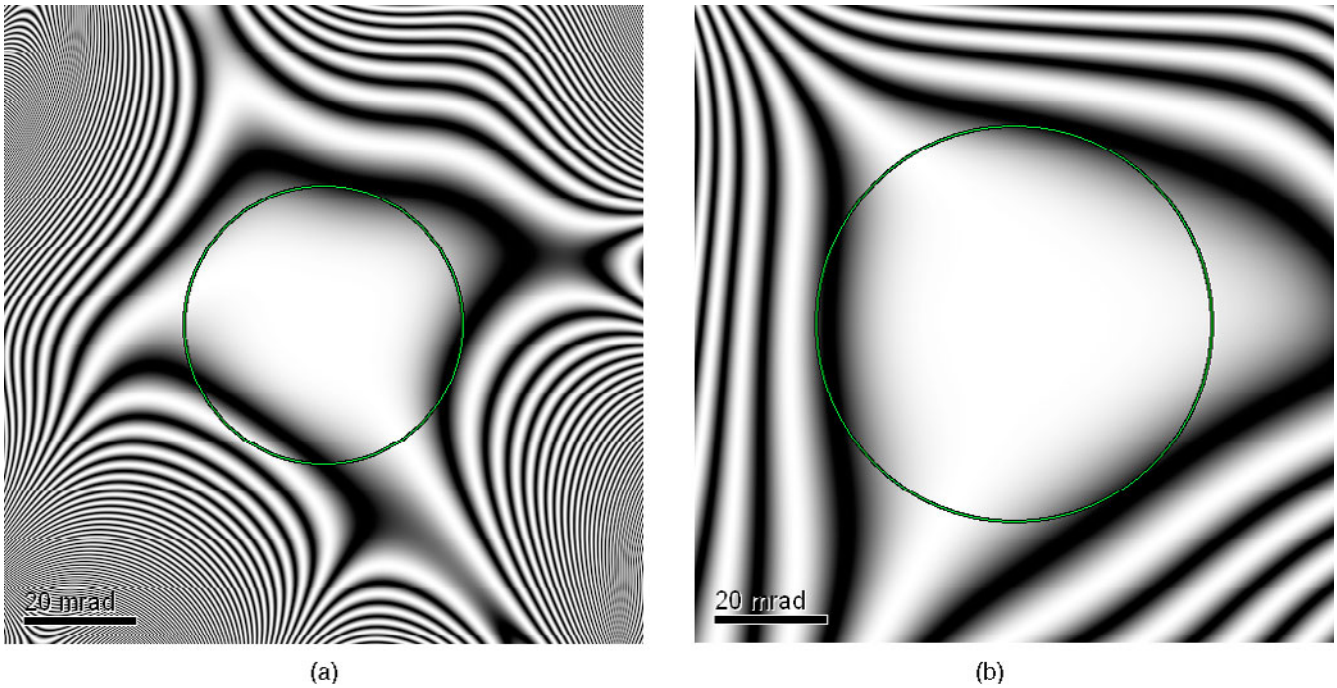

Figure 1. Phase-shift images calculated from measured aberrations for (**a**) the CESCOR and (**b**) the DCOR. The approximate size of the corrected area is indicated by 25 and 35 mrad (half-angle) apertures, respectively. The first-order aberrations (C_1 and A_1) were manually set to zero.

to about 0.78 Å with this system (Lupini & Pennycook, 2008*a*).

To reduce A_5, CEOS designed and constructed an improved corrector with shorter, stronger hexapoles and additional multipole coils (Müller et al., 2006), which was installed at ORNL in 2007. The extra multipole coils include long quadrupoles that allow more flexibility for the reduction of third- and fourth-order aberrations. Thus the DCOR would be expected to provide significantly lower parasitic and nonround fifth-order aberrations. The software was also improved to allow the use of larger tilt angles during measurement, thereby improving the potential measurement accuracy. Using the improved DCOR, we were able to reduce C_5 to below 0.5 mm and typically measure A_5 below about 0.1 mm (see Table 1 for examples). Both of these values reflect the measurement accuracy because C_5 should be close to zero in both correctors and A_5 about 0.2 mm in the improved DCOR (Müller et al., 2006). The chromatic aberration (C_c) of the system was measured (Lupini & Pennycook, 2008*b*) as about 2.4 mm (2 mm relativistically adjusted), although in Z-contrast STEM we expect this to increase the probe tails rather than limit the two-dimensional (2D) resolution. Other similar projects are under way to produce improved QO-style correctors (Krivanek et al., 2008*b*) and to include C_c correction (Haider et al., 2008).

Table 1. Typical Measured Values in nm of the Residual Aberrations for the DCOR and the CESCOR.*

Aberration	DCOR	Standard Deviation	CESCOR	Standard Deviation
C1	−2.2	1.6	−1.4	3.7
A1	2.2	1.1	0.6	0.4
A2	13.3	7.5	75.8	18.9
B2	20.2	10.6	71.6	16.9
C3	−545	478	−1,066	1,634
A3	304	238	1,837	701
S3	315	155	1,815	372
A4	1,771	622	60,564	8,239
D4	2,558	437	19,901	6,432
B4	2,985	1,062	14,802	9,731
C5	163,744	84,410	2,482,550	2,551,793
A5	28,705	12,882	1,715,875	314,898
R5	14,324	6,512		
S5	43,369	17,019		

*The values are averaged over eight successive measurements, and the standard deviation is shown (rather than the 95% limits reported by the software).

Results and Discussion

A prerequisite for high-resolution TEM is that the stability of the column must be sufficient to allow the desired resolution. Instabilities are frequently seen in STEM images

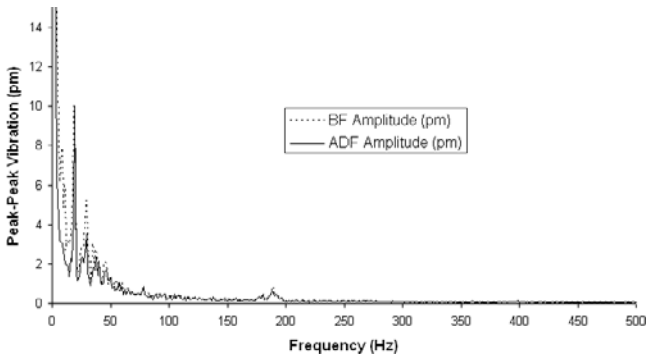

Figure 2. Representative spot spectra recorded on the Titan S. A calibrated 10 pm peak to peak sine wave wobble at 20 Hz was applied and used to scale the amplitudes. No other significant features were seen up to 1200 Hz, after the turbo pump was isolated from the column.

as jagged edges on the atomic columns because the probe is scanned across the sample over a finite time. This differs from a TEM image, where all the pixels are acquired simultaneously and the instabilities produce a more general contrast damping. The sensitivity of the STEM image to instabilities provides a convenient method to measure the stability of the whole column. Figure 2 shows the Fourier transform of an image taken without scanning the probe. Any change in contrast is therefore due to an undesired motion of the sample or the probe and thus represents the overall stability of the column. The difficulty is that the amplitude scale would be uncalibrated, so a 10 pm wobble at 20 Hz was applied using an alignment control and used to calibrate the vertical scale. This figure illustrates that the overall stability of the column is below 10 pm for all frequencies above a few Hz. Some low-frequency instabilities and drifts were observed, particularly after moving the sample and from thermal or pressure fluctuations in the room, which highlights the importance of a high-quality environment.

2D and 3D Resolution

Figure 3 shows a STEM image of hexagonal GaN viewed down the [211] axis taken on the ORNL Titan S column. The Fourier transform reveals that the spot corresponding to the 0.63 Å (306) spacing is present and significantly above the noise, which is a necessary but not sufficient condition to claim a particular resolution (O'Keefe & Allard, 2004). The relationship between information transfer and resolution has been considered previously (for example, O'Keefe & Allard, 2004; Peng et al., 2008 and references therein). The two Ga columns forming the "dumbbell" are generally resolvable over the whole field of view. More quantitatively, averaging over the image, the dip between Ga dumbbells is about 8% of the minima between dumbbell pairs. On the basis of this figure and considering the measured characteristics (aberrations, stabilities, and brightness), the Titan at ORNL exceeds the Sparrow criterion, but not the more stringent Rayleigh criterion, for a resolution of 0.63 Å. It is also interesting to observe the asymmetry in the linetrace, which appears to show a slight tail on the left of the bright Ga columns, at the positions of the N columns. We physically rotated the sample in the holder and confirmed that this tail was repeatable, suggesting it is not just an artifact due to mistilt or residual aberrations. Although the N columns are not resolved here, this observation shows how aberration-corrected instruments are beginning to allow even light columns to be resolved in Z-contrast imaging (Chisholm et al., 2004).

In STEM, the optimal size for the probe-forming aperture α is conventionally chosen as a balance between the effects of aberrations and the diffraction limit. The contributions from the geometric aberrations increase at higher angles, favoring the use of a small aperture, while diffraction favors the use of a large aperture. In an uncorrected system, this restriction on aperture size has conventionally meant that the diffraction limited depth of field is relatively large. The correction of the lens aberrations has allowed the use of larger apertures, with subsequent reductions in the depth of field, as well as the lateral resolution. Acquiring a series of images with a small focus step between frames, therefore, allows 3D information to be obtained (Borisevich et al., 2006*a*; van Benthem et al., 2006).

This type of image formation in a STEM looks very much like a confocal optical microscope, but we do not use a pinhole aperture in a confocal plane. Several workers have proposed the use of electron-optical systems that more closely resemble a confocal microscope (Einspahr & Voyles, 2006; Nellist et al., 2006), which may offer improved vertical resolution. In a purely diffraction limited system, the depth of field Δz is commonly defined as

$$\Delta z_R = 2\,\frac{\lambda}{\alpha^2}, \tag{2}$$

where the prefactor depends on the sometimes tricky question of how exactly resolution is defined. Although several different definitions are used, equation (2) corresponds conveniently to a Rayleigh-type criterion (the distance from the maximum to the first minimum) and λ is the wavelength. Another factor that will limit the depth of field is the chromatic spreading of focus due to the different electron energies. Ignoring relativistic effects, the focus change due to chromatic aberration is

$$\Delta z_{Cc} = C_c\,\frac{\Delta E}{E}. \tag{3}$$

Figure 4 shows the probe size plotted using approximate values for an uncorrected Titan, a corrected but perfectly monochromatic machine, and a realistic corrected

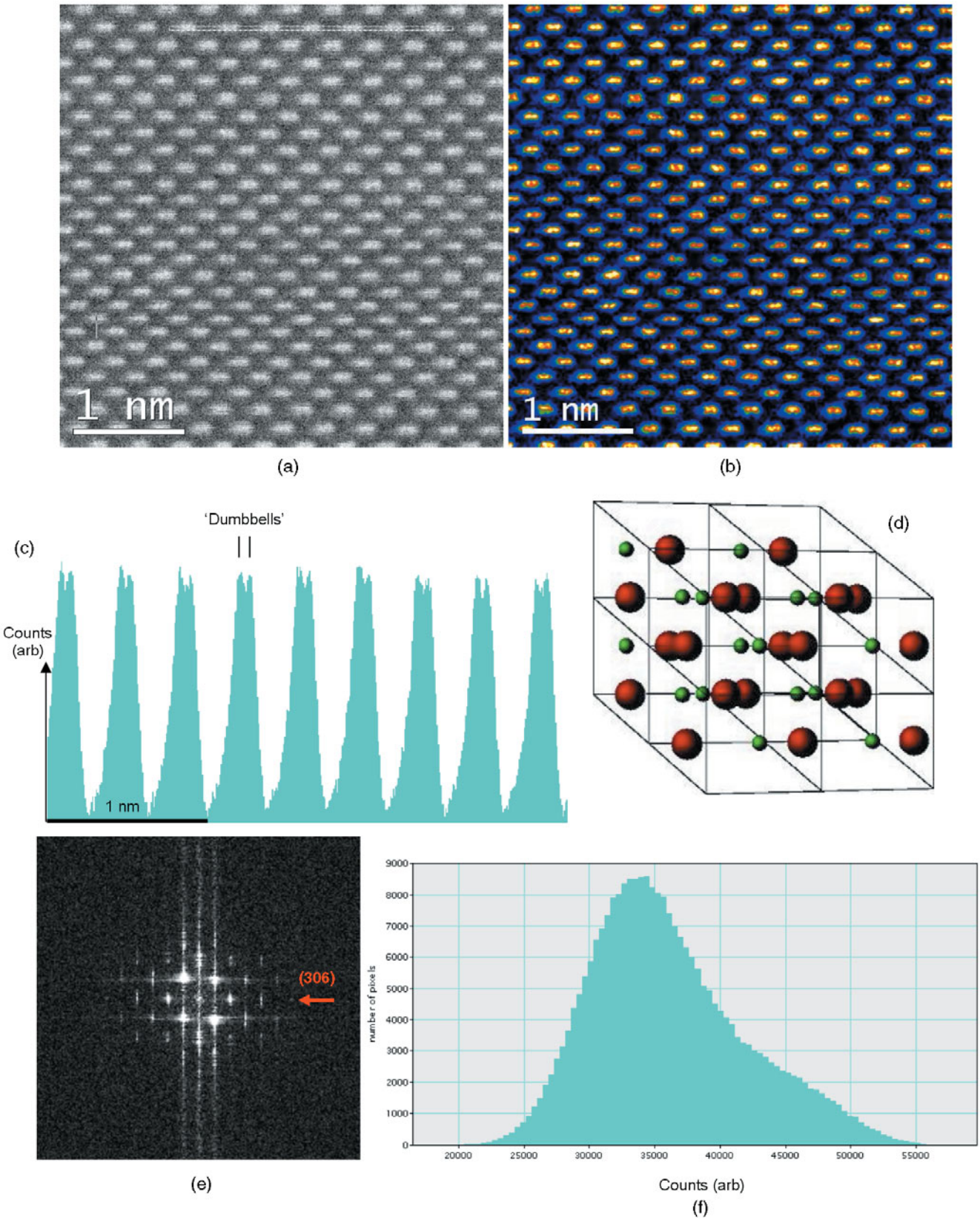

Figure 3. Example Z-contrast image of GaN [211], sample courtesy of J.G. Wen and I. Petrov of the University of Illinois at Urbana-Champaign. (**a**) Raw data; (**b**) low-pass filtered and colorized; (**c**) an averaged linetrace across 26 rows from the image, using regions equivalent to the one marked on the raw data; (**d**) the atomic positions (not to scale) with Ga in red and N in green; (**e**) the Fourier transform; (**f**) the histogram, confirming that the data are not "clipped."

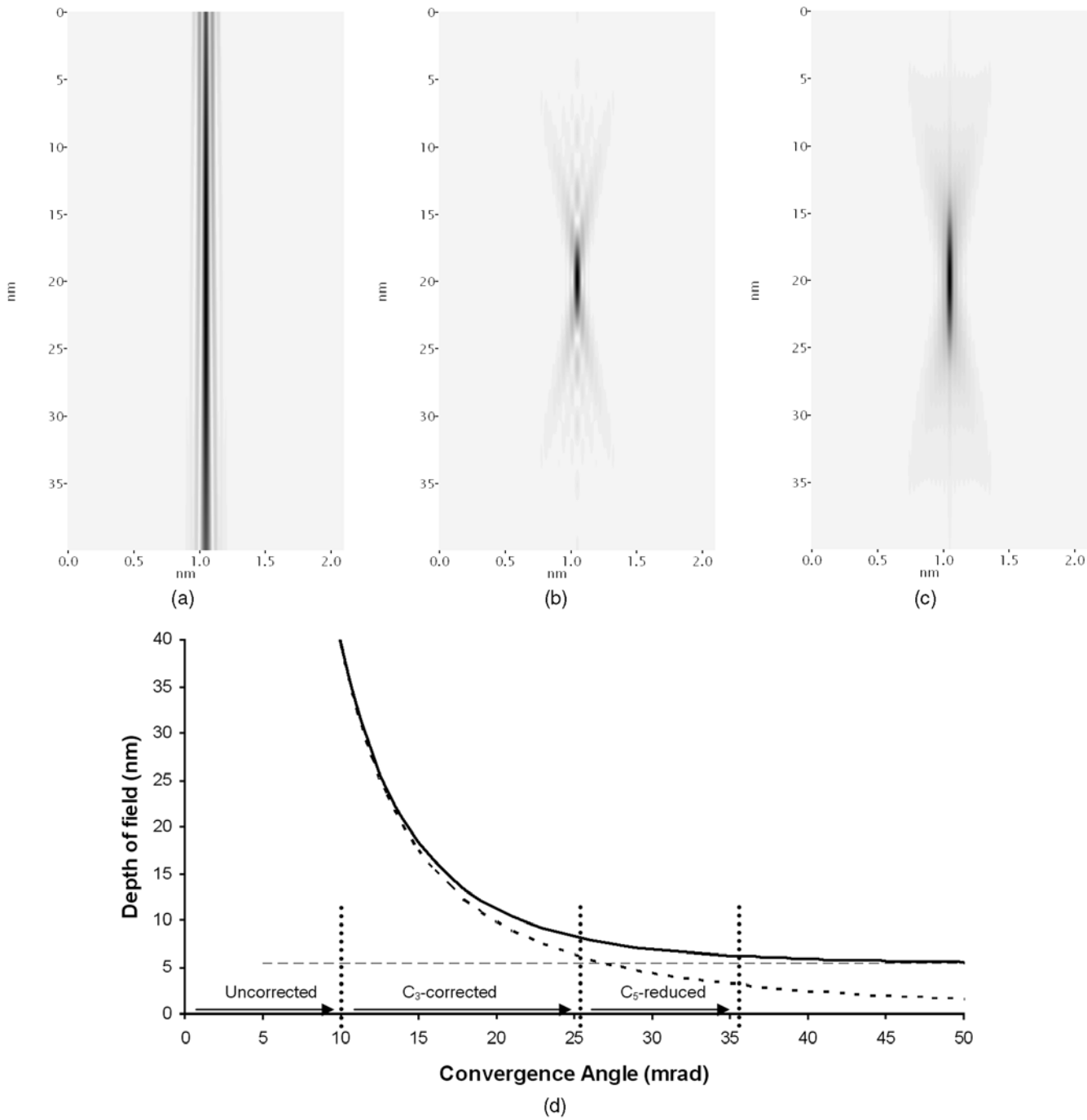

Figure 4. Calculated 3D probes for a STEM with (**a**) $C_s = 1.22$ mm, 10 mrad; (**b**) $C_s = 0$ mm, 30 mrad; (**c**) $C_s = 0$ mm, 30 mrad, $C_c = 2$ mm, $\Delta E = 0.8$ eV. (**d**) Depth of field as a function of convergence angle (solid) showing contributions for a pure diffraction limit (dashed) and a pure chromatic aberration limit (dashed horizontal). Approximate values for the FEI Titan at 300 kV are assumed ($C_c = 2$ mm and $\Delta E = 0.8$ eV). Dotted vertical lines indicate the approximate range of usable apertures for different levels of aberration correction.

probe with chromatic aberration and fractional energy spread $\Delta E/E$ included. Because the chromatic and geometrical depths of field are largely independent, it is possible to estimate their relative contributions by adding in quadrature. Plotting out the expected behavior using values from the FEI Titan 80-300 at ORNL reveals something very interesting. At low convergence angles, the depth of field is limited by diffraction, while at around 25–30 mrad the depth of field begins to be limited by the chromatic focus spread. In practice, for high-resolution 2D STEM work, we

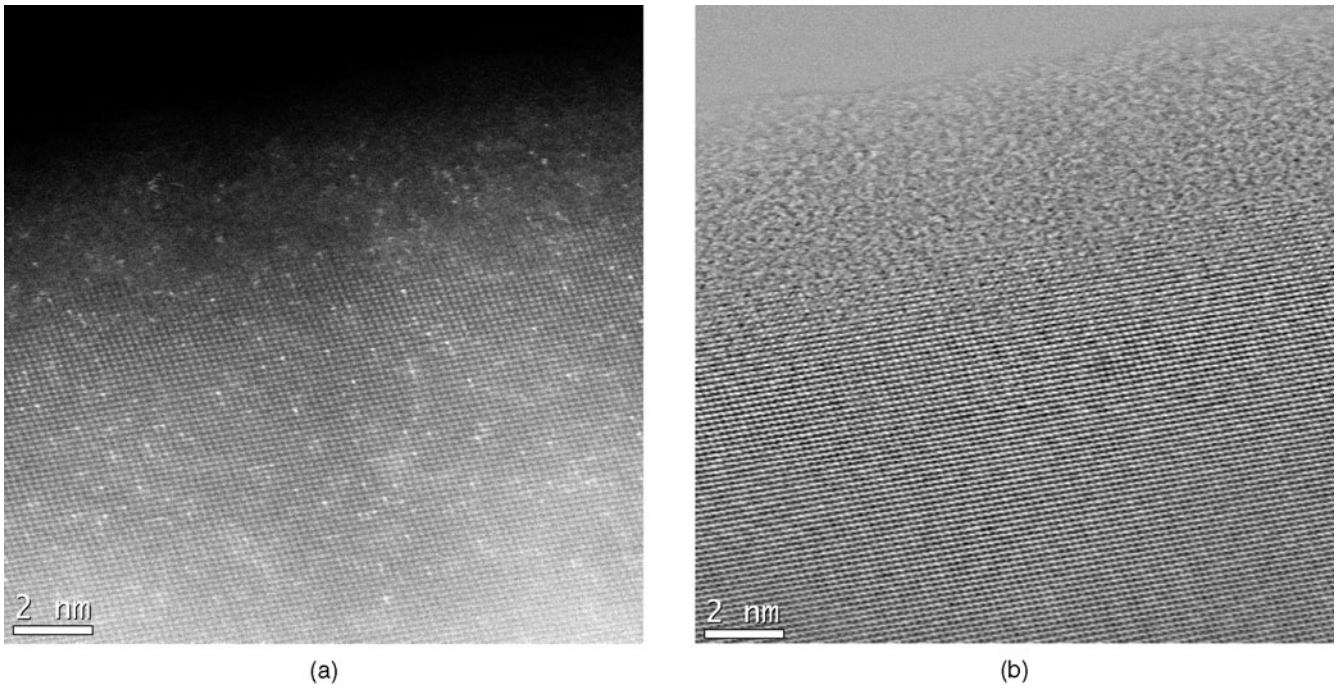

Figure 5. Simultaneously acquired (**a**) Z-contrast and (**b**) BF images of a Si sample ion-implanted with Bi atoms.

found that convergence angles in exactly this range gave the best images with the improved DCOR. Our default high-resolution imaging setting presently starts with a 27.5 mrad convergence angle. Since the full vertical resolution of 3D STEM is only likely to be approached for point-like objects, we investigated samples containing single dopant atoms to probe the resolution limits.

Detection of Single Bi Atoms

The ability to detect single dopant atoms can be very important in the analysis of modern nanodevices and electronics. An advantage of Z-contrast STEM is that it can be sensitive to single heavy dopant atoms on or in a relatively thick support if the difference in atomic number is large enough (Voyles et al., 2002; Lupini & Pennycook, 2003). Silicon forms the basis for almost all modern microelectronics, so here we investigate the prospects for single atom detection with 3D sensitivity in a doped Si sample. Figure 5 shows an image of a Si sample ion-implanted with Bi atoms viewed down the [100] axis. The simultaneously acquired, and also aberration-corrected, BF image reveals the presence of an amorphous region at the edge of the sample, while the single Bi atoms are obvious in the Z-contrast image. It is not clear from this single image if the atoms are in or on the sample, meaning that 3D information is required.

Figure 6 shows extracted frames from a through-focus series obtained by changing the objective lens in 4 nm steps. The series reveals that different Bi atoms come into focus in different frames, demonstrating that they are at different depths within the sample. The chart shows the excess intensity above the background for three selected atoms as a function of focus. Despite the low probe current (about 100 pA), some of the Bi atoms in this sample were very mobile, probably due to the high-voltage used (300 kV). The mobile Bi atoms made it hard to determine whether the dopants were going out of focus or were just displaced by the beam. A qualitative observation is that the more mobile atoms appeared in focus at different fames from the fixed Bi atoms. It is therefore probable that the mobile Bi atoms are on the surface or in the amorphous layer, while those that did not move are more likely to be trapped in the bulk, where they will not be able to move so easily. The mobile Bi made it more difficult to find the same atom in multiple frames. However, the independent motion of the mobile Bi atoms provides convincing evidence that they are indeed single atoms and therefore acts as a convenient intensity calibration to confirm that the Bi atoms inside the crystal are also single atoms. Thus, although this sample clearly contained single dopant atoms, we next sought a sample with less mobile dopants and decided to use smaller focal steps.

Detection of Single La Atoms

Figure 7 shows an image of a cross-section sample with a $CaTiO_3$ layer grown on a $SrTiO_3$ substrate. The $CaTiO_3$ layer was grown in three parts, starting with a nominal thickness of 26 unit cells (about 10 nm), then half a mono-

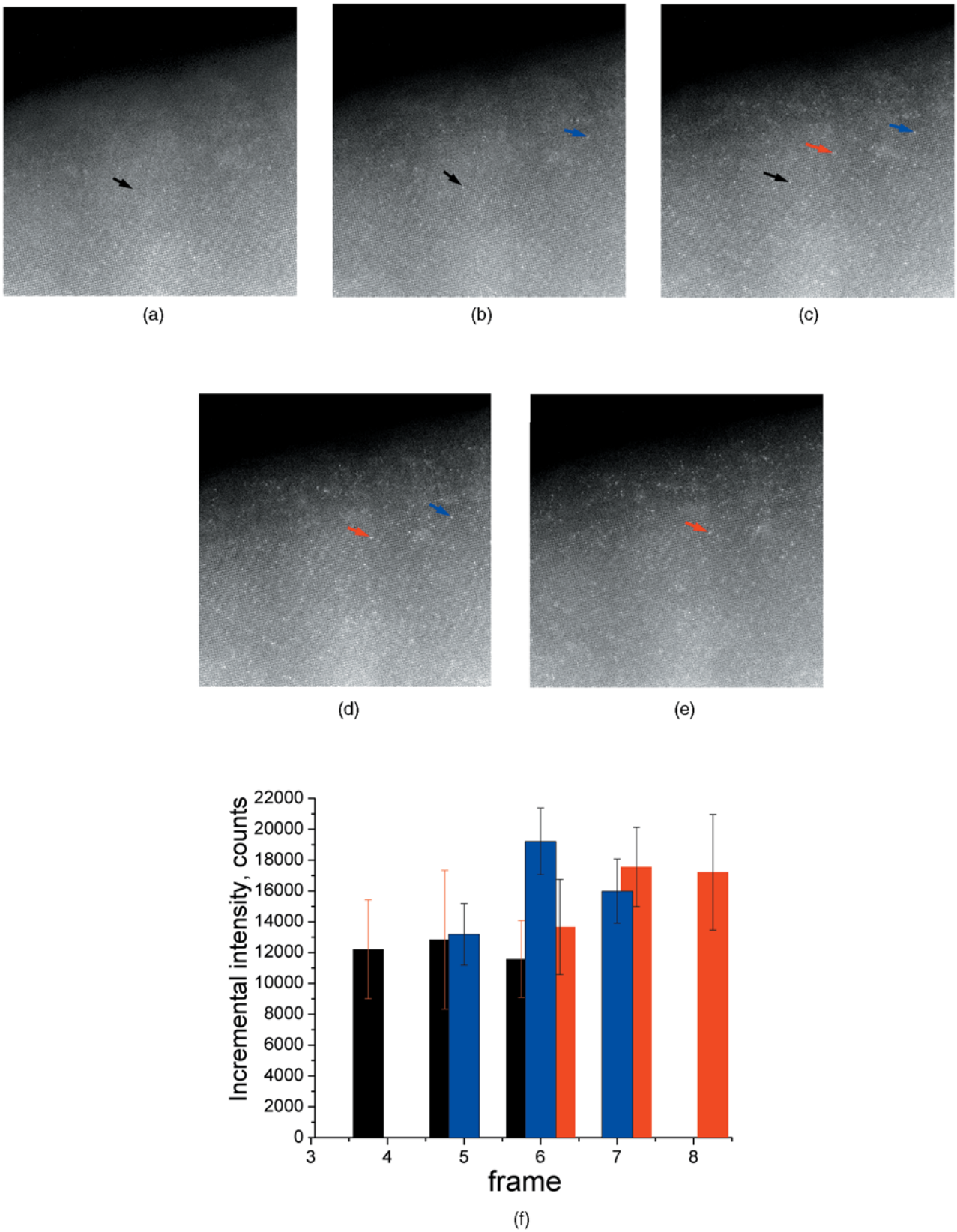

Figure 6. a–e: Extracts from selected frames from a through-focus series showing a Si sample ion-implanted with Bi atoms. The frames are separated by 4 nm vertically. **f:** The incremental intensity of the selected Bi atoms above the nearby background were extracted and plotted as a function of focus. Different atoms come into focus at different planes. Each selected atom was visible over three frames.

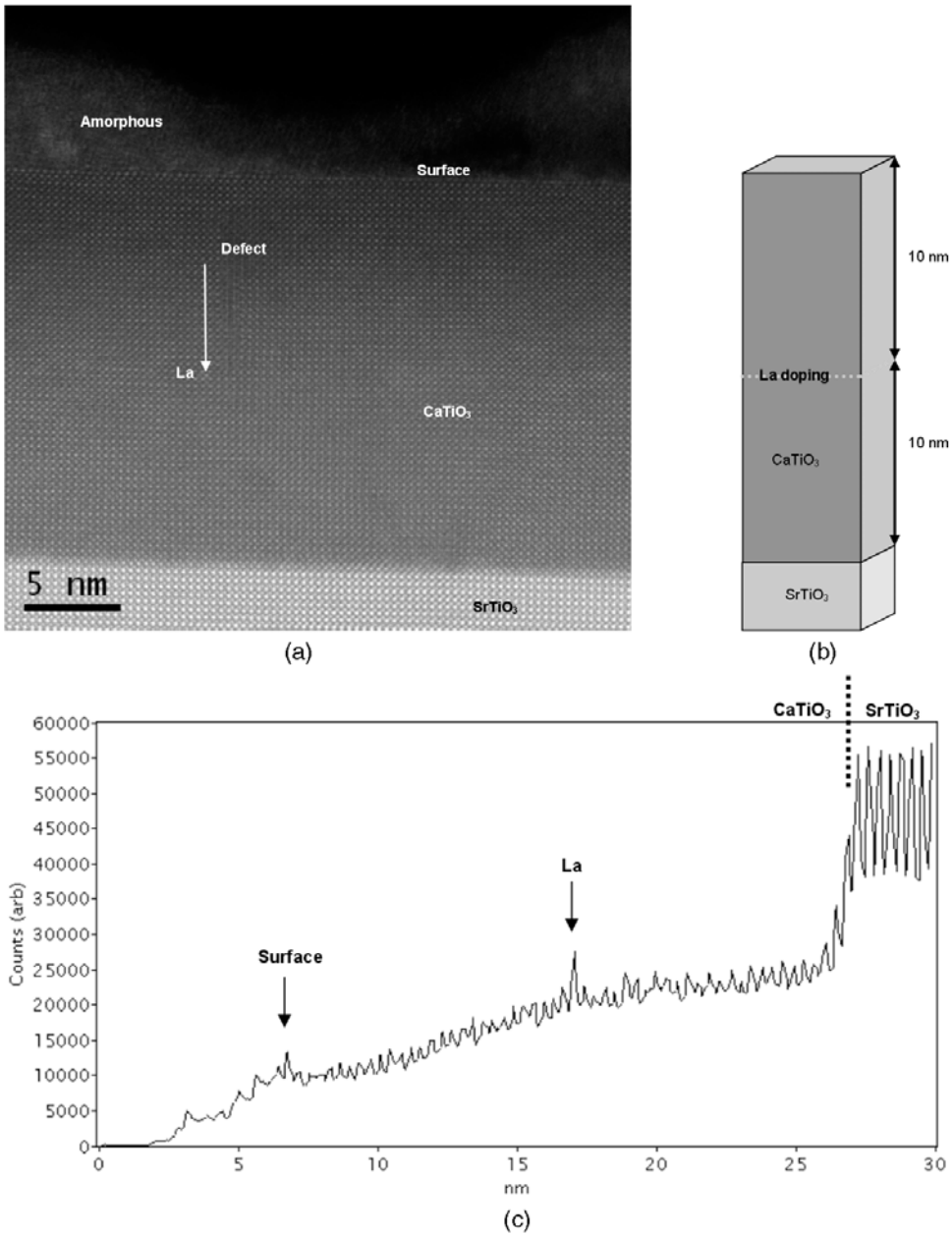

Figure 7. **a:** Z-contrast image of the $CaTiO_3$ layer showing the $SrTiO_3$ substrate at the bottom and an amorphous layer, then vacuum at the top. A single La doped column is indicated. **b:** Nominal sample composition. **c:** A linetrace along the direction of the arrow shown reveals the La column sitting at about 10 nm from both the surface and the substrate.

layer doped with 5% La, then another nominal 25.5 unit cells (about 10 nm) as a capping layer. It is expected that the La atoms will substitute for the Ca atoms. In a different sample, by using layers with varying dopant concentrations, single La atoms have been previously detected using EELS (Varela et al., 2004).

We can construct a simple model for the doping, assuming an idealized sample growth with the La randomly distributed in a single flat monolayer. Under this assumption, a plan-view sample will have at most one La atom per column. Here, we used a cross-section sample, which will potentially have more than one La atom per column, but has the advantage that the distance from the substrate or surface can be used as an additional criterion for confirming La detection. For a cross-section sample, the number of La atoms in a column will approximately follow a binomial distribution. If we have n potential sites and a doping probability p, the probability P of finding r La atoms will be

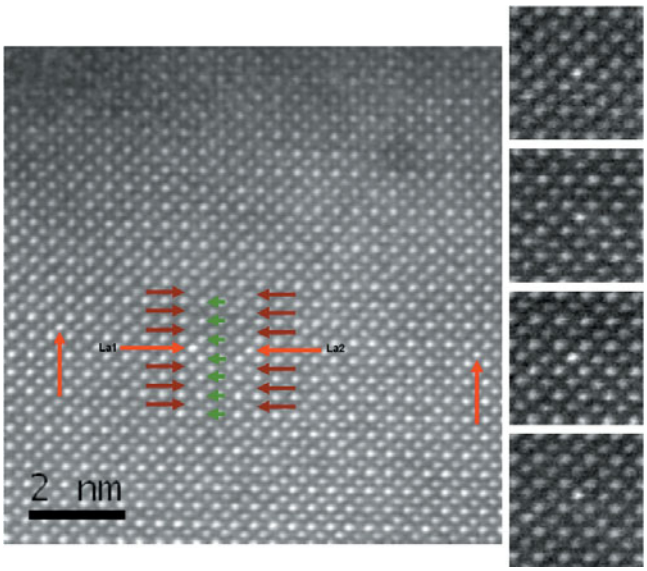

Figure 8. Extract (low-pass filtered) from a through focus series showing four prospective La doped columns (large, red arrows). The medium (red) arrows indicate the Ca columns used to extract the Ca intensities and the small (green) arrows indicate the Ti columns used to extract the Ti intensities. (Right) Magnified raw data with the contrast scaled, around the brightest La column in four frames close to focus (2 nm steps).

$$P(r) = \frac{n!}{r!(n-r)!} p^r (1-p)^{n-r}. \quad (4)$$

Thus for a monolayer concentration of 2.5% in a sample that is about 10 unit cells thick, we expect about 78% of the columns to have no La atoms, 20% to have one La atom, and 2% to have more than one. For a 10 unit cell thick sample, we can be 98% certain that any particular column contains one or fewer La atoms. A quantitative estimate of the sample thickness is difficult, because there is an amorphous damaged layer on both surfaces of the sample and probably some contamination. For a hypothetical thin sample, the intensity would reveal the number of La atoms in a straightforward manner. However, in a thick aligned crystal, the intensity will depend on the depth of the La atom within the crystal, as discussed below.

The La atoms were difficult to spot in the presence of imperfections, such as surface roughness and sample drift. One experimental trick that helped to keep track of the same column was to find a dopant near a defect (as in Fig. 7). For the current densities used in imaging, the La atoms were not observed to move. Because surface atoms in the amorphous region were clearly observed to move, this provides evidence that the La atoms were in the bulk. Figure 8 shows an extract from a focal series taken with 2 nm steps. About four likely La sites are visible (around 15% of the 26 columns) with one site displaced a unit cell above the plane of the others. Because the convincing candidate La atoms were found to be within ± 1 unit cell of the central plane (about 10 nm from the top and bottom surfaces), it appears that the film growth was precise. This provides further evidence that the La atoms examined had remained inside the film because redeposition on the surface during sample preparation would also involve lateral translation.

The other question to address is whether the detected La-doped columns contained single or multiple atoms. One useful calibration is obtained from the single atoms in the amorphous region. The brightest atoms are almost certain to be Sr (since the overall La atomic percentage is insignificant). Extracting the maximum from these atoms suggests that a single Sr atom gives about 6,000 counts over the amorphous background which is mostly glue. The brightest La column found in the series gave about 12,000 counts above the Ca columns, which suggests that this extra La is twice as bright as a Sr atom. This difference seems consistent with the ratio of atomic numbers Z_{La} to Z_{Sr}, which is 57:38, assuming that the intensity will vary approximately as Z^2. Other prospective La atoms were less bright, presumably corresponding to different depths within the sample. Thus the intensities are in the range consistent with columns containing one La atom, although multiple atoms cannot be entirely discounted.

The intensity obtained on changing the focus is shown in Figure 9 for several selected columns. It is clear that the bright columns believed to contain La are significantly brighter than the nearby Ca columns over the whole focus range. The variation of the nearby columns confirms that the intensity change is too large to be due to a simple change in thickness or surface reconstruction. We finally turned to image simulations to provide a more quantitative interpretation of these results.

Calculations

To investigate the effects of changing focus on the intensities, multislice calculations were performed using the code provided by Kirkland (1998). Because of the large incident angles required, large supercells of 2,048 × 2,048 pixels were used, corresponding to 32.6 × 32.6 Å (Si [100]) and 38.2 × 38.2 Å ($CaTiO_3$ [100]) at a real space resolution of 0.04773 Å (412 mrad) for Si and 0.05598 Å (352 mrad) for $CaTiO_3$. Each slice was 1.36 Å thick for Si and 1.91 Å for $CaTiO_3$. A probe convergence angle of 27.5 mrad, a residual C_5 of 0.5 mm, and a detector inner angle of 65 mrad were used, which were close to the experimental conditions. Chromatic focus changes and phonons were not included in order to reduce the necessary computer time. As the curves were smooth, these omissions would spread the depth of focus but not dramatically change the shape.

The intensity curve in Figure 10 suggests that some degree of depth sensitivity is possible in Si [100]. While the full-width at half-maximum of about 4 nm is consistent

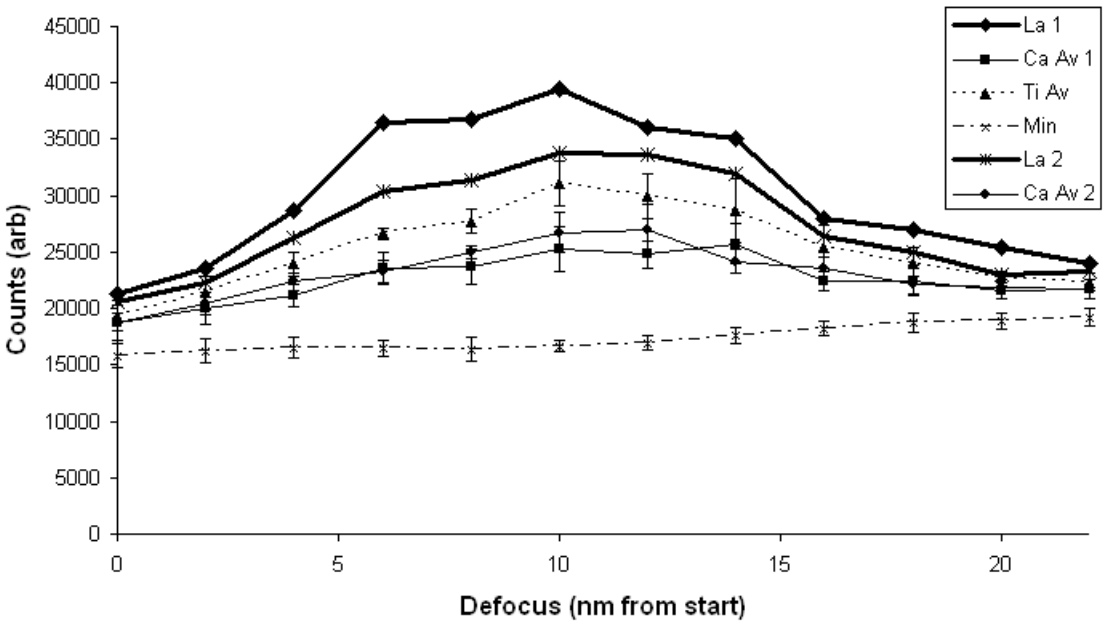

Figure 9. Absolute counts in the Z-contrast image as a function of defocus for selected columns taken from the series in Figure 8. La 1 and La 2 are two columns that clearly contain La atoms. Ca average 1 and 2 are the averages of the six Ca columns near to each La (three above and three below, as shown in Fig. 8), and the error bars are the standard deviations. Ti is the average of the seven Ti columns marked, and Min is the background measured in the same way.

with the experimental observation that the atoms were visible over only three frames (an 8 nm range), the experimental curves were noticeably flatter than expected from the calculation. The experimental depth of field was difficult to measure accurately because of the mobile Bi atoms, even though not all of the Bi atoms were mobile. Work is under way to repeat similar experiments with different microscope settings to further investigate the depth dependence of the signal. It seems likely that factors not included in the simulation, such as the movement of the Bi atoms, chromatic aberration, and the substantial amorphous surface layer, will affect the contrast.

The $CaTiO_3$ sample had the experimental advantage that most of the La atoms were not mobile and were found to be visible over a larger range of focus. However, there was very little depth sensitivity within the crystal from changing focus. This result is confirmed by the calculations. Figure 10 reveals that the changes in the excess intensity from the La atoms depend on the depth of the dopant within the crystal more strongly than on the focus used. The problem is that for convergence angles less than about 35 mrad, the channeling effect will still be significant in $CaTiO_3$ (Borisevich et al., 2006*b*). Using larger convergence angles would improve the depth sensitivity to focus changes, although without C_c correction or monochromation, the chromatic aberration will be a limiting factor. Figure 10 also reveals that the extra intensity due to a single La atom will change by a large factor with depth even in these thin samples. A single La atom near the entrance surface gave a smaller signal than one at a depth of 4 nm for all focus planes under these conditions. Examining Figure 10 suggests that the extra signal due to the La can vary between 10 to 90% of the Ca column signal over this range of sample thickness, depending on the depth of the dopant within the column. Intensities at the lower end of this range are difficult to distinguish from the random fluctuations of the Ca columns, which were of a similar magnitude due to contamination and surface damage. (The two La columns in Fig. 9 were about 56 and 26% brighter than nearby Ca columns.) Thus, only atoms within a particular depth range can be easily distinguished from the nearby Ca columns, meaning that the number of La atoms detectable by eye will probably underestimate the true number present in the sample.

Conclusions

We have presented some initial results from the FEI Titan 80-300 installed at ORNL as part of the DOE TEAM program. A resolution of 0.63 Å has been demonstrated in GaN [211]. Although that particular image was the result of substantial optimization, information transfer to about 0.8 Å is becoming routine. The detection of single heavy dopant atoms has been examined and the dependence of the signal on focus was observed, meaning that some 3D information is being extracted. Calculations indicated that the apertures used were probably too small to optimize the high-resolution

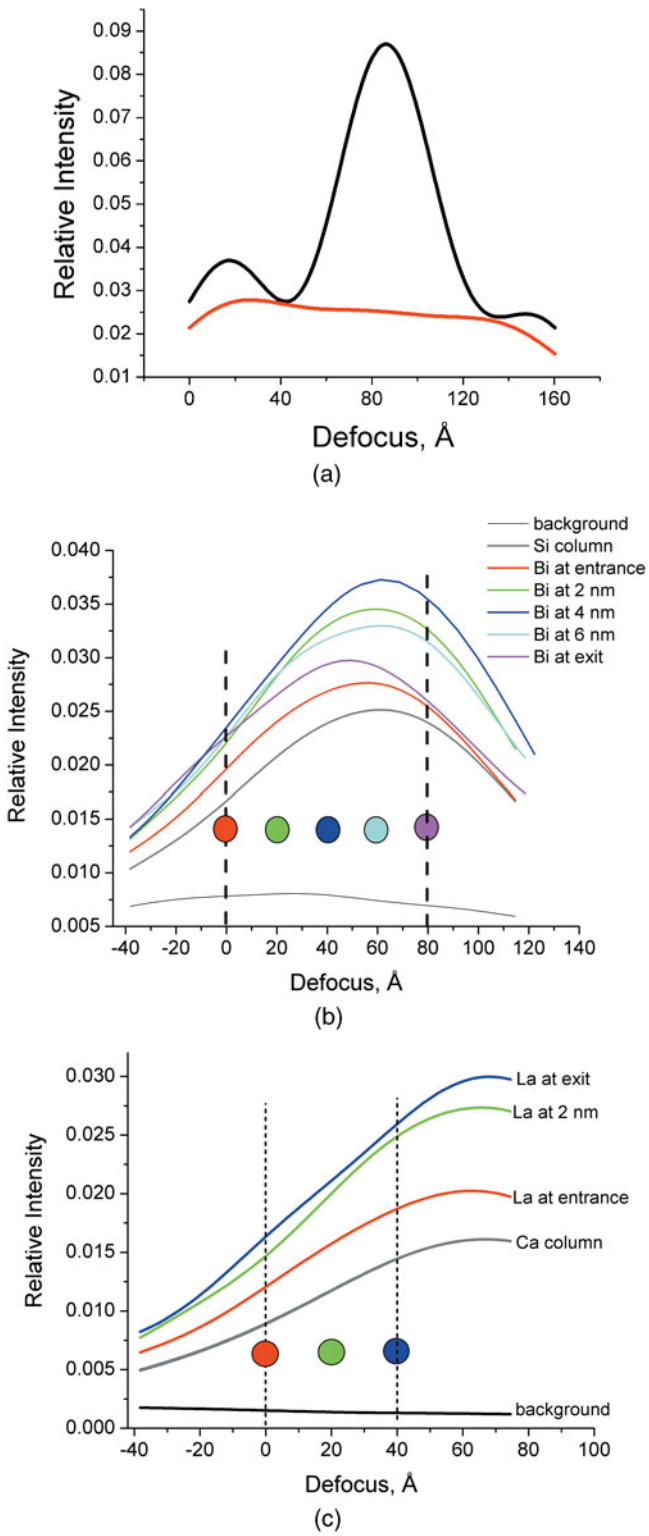

Figure 10. Multislice simulations showing the relative intensity for dopant atoms inside aligned crystals. Convergence angle 27.5 mrad, at 300 kV, residual C_5 = 0.5 mm, detector 65 to 300 mrad. **a:** Bi atom in 16 nm Si [100] (Bi 8 nm deep) for a doped (black) and undoped (red) column. **b:** Single La atoms in 7.6 nm $CaTiO_3$ [100] at different depths as indicated. **c:** Single La atoms in 3.8 nm $CaTiO_3$ [100] at different depths as indicated. Note different scales.

3D information. One problem is that to get a good signal-to-noise ratio over the background, it was necessary to use thin samples that had a thickness similar to the depth of field. Improvements in the signal-to-noise ratio would allow thicker samples and reducing the residual aberrations further would allow the use of larger convergence angles. Therefore, these results indicate the need for further instrumental improvements to provide better depth resolution even in cases where there is no obvious need merely for higher lateral resolution. The effect of chromatic aberration as a resolution limit in the vertical direction also suggests that monochromation, chromatic aberration correction, and improved sources will also offer benefits for 3D imaging techniques.

Acknowledgments

The research was supported by the Division of Materials Science and Engineering of the U.S. Department of Energy (DOE) at Oak Ridge National Laboratory, managed by UT-Battelle. The instrumentation used in this research was provided as part of the TEAM project, funded by the DOE Office of Science. The authors are grateful to Dr. J.G. Wen and Dr. I. Petrov for preparing the high quality GaN sample. Critical reading of this manuscript by Drs. E.A. Kenik, M. Watanabe, Q.M. Ramasse, and R. Erni, and instrumentation development by FEI Co. and CEOS GmbH are gratefully acknowledged.

References

Beck, V. (1979). Hexapole spherical-aberration corrector. *Optik* **53**, 241–245.

Borisevich, A.Y., Lupini, A.R. & Pennycook, S.J. (2006*a*). Depth sectioning with the aberration-corrected scanning transmission electron microscope. *Proc Nat Acad Sci* **103**(9), 3044–3048.

Borisevich, A.Y., Lupini, A.R., Travaglini, S. & Pennycook, S.J. (2006*b*). Depth sectioning of aligned crystals with the aberration-corrected scanning transmission electron microscope. *J Elec Micros* **55**(1), 7–12.

Chisholm, M.F., Lupini, A.R., Pennycook, S.J., Ohkubo, I., Christen, H.M., Findlay, S.D., Oxley, M.P. & Allen, L.J. (2004). Simultaneous Z-contrast and phase contrast imaging of oxygen in ceramic interfaces. *Microsc Microanal* **10**(Suppl 2), 256–257.

Crewe, A.V. & Kopf, D. (1980). A sextupole system for the correction of spherical aberration. *Optik* **55**, 1–10.

Dellby, N., Krivanek, O.L., Nellist, P.D., Batson, P.E. & Lupini, A.R. (2001). Progress in aberration-corrected scanning transmission electron microscopy. *J Electr Microsc* **50**, 177–185.

Einspahr, J.J. & Voyles, P.M. (2006). Prospects for 3D, nanometer-resolution imaging by confocal STEM. *Ultramicroscopy* **106**, 1041.

Haider, M., Müller, H., Uhlemann, S., Zach, J., Loebau, U. & Hoeschen, R. (2008). Prerequisites for a Cc/Cs-corrected ultrahigh-resolution TEM. *Ultramicroscopy* **108**, 167–178.

Hartel, P., Müller, H., Uhlemann, S. & Haider, M. (2004). Residual aberrations of hexapole-type Cs-correctors. In *Proceedings of the 13th European Microscopy Congress*, Van Dyck, D. & Oostveldt, P. (Eds.), vol. I, pp. 41–42. Antwerp: The Belgian Society for Microscopy.

Hawkes, P.W. & Kasper, E. (1996). *Principles of Electron Optics*. Vol. 2, pp. 857–863. New York: Academic Press.

Kirkland, E.J. (1998). *Advanced Computing in Electron Microscopy*. New York: Plenum Press.

Kisielowski, C., Freitag, B., Bischoff, M., Van Lin, H., Lazar, S., Knippels, G., Tiemeijer, P., Van Der Stam, M., Von Harrach, S., Stekelenburg, M., Haider, M., Uhlemann, S., Müller, H., Hartel, P., Kabius, B., Miler, D., Petrov, I., Olson, E.A., Donchev, T., Kenik, E.A., Lupini, A.R., Bentley, J., Pennycook, S.J., Anderson, I.M., Minor, A.M., Schmid, A.K., Duden, T., Radmilovic, V., Ramasse, Q.M., Watanabe, M., Erni, R., Stach, E.A., Denes, P. & Dahmen, U. (2008). Detection of single atoms and buried defects in three dimensions by aberration-corrected electron microscope with 0.5-Å information limit. *Microsc Microanal* **14**, 469–477.

Koops, H. (1978). Aberration correction in electron microscopy. In *Electron Microscopy*, Sturgess, J.M. (Ed.), Vol. 3, pp. 185–196. Toronto: Microscopical Society of Canada.

Krivanek, O.L., Corbin, G.J., Dellby, N., Elston, B.F., Keyse, R.J., Murfitt, M.F., Own, C.S., Szilagyi, Z.S. & Woodruff, J.W. (2008*a*). An electron microscope for the aberration-corrected era. *Ultramicroscopy* **108**, 179–195.

Krivanek, O.L., Dellby, N., Keyse, R.J., Murfitt, M.F., Own, C.S. & Szilagyi, Z.S. (2008*b*). Advances in aberration-corrected scanning transmission electron microscopy and electron energy-loss spectroscopy. In *Advances in Imaging and Electron Physics*, Hawkes, P.W. (Ed.), Vol. 153, pp. 1–41. New York: Academic Press.

Krivanek, O.L., Dellby, N. & Lupini, A.R. (1999). Towards sub-Å electron beams. *Ultramicroscopy* **78**, 1–11.

Lentzen, M. (2006). Progress in aberration-corrected hight-resolution transmission electron microscopy using hardware aberration correction. *Microsc Microanal* **12**, 191–205.

Lupini, A.R. & Pennycook, S.J. (2003). Localization in elastic and inelastic scattering. *Ultramicroscopy* **96**, 313–322.

Lupini, A.R. & Pennycook, S.J. (2008*a*). Aberration corrected imaging in the STEM. *Microsc Microanal* **13**(Suppl. 2), 1146–1147.

Lupini, A.R. & Pennycook, S.J. (2008*b*). Rapid autotuning for crystalline specimens from an inline hologram. *J Elec Micros* **57**, 195–201.

Lupini, A.R., Rashkeev, S.N., Varela, M., Borisevich, A.Y., Oxley, M.P., Van Benthem, K., Peng, Y., De Jonge, N., Veith, G.M., Pantelides, S.T., Chisholm, M.F. & Pennycook, S.J. (2007). Scanning transmission electron microscopy. In *Nanocharacterization*, Kirkland, A.I. & Hutchison, J.L. (Eds.), pp. 28–65. London: The Royal Society of Chemistry.

Müller, H., Uhlemann, S., Hartel, P. & Haider, M. (2006). Advancing the hexapole Cs-corrector for the scanning transmission electron microscope. *Microsc Microanal* **12**, 443–455.

Nellist, P.D., Behan, G., Kirkland, A.I. & Hetherington, C.J.D. (2006). Confocal operation of a transmission electron microscope with two aberration correctors. *Appl Phys Lett* **89**, 124105.

O'Keefe, M.A. & Allard, L.F. (2004). A standard for subÅngström metrology of resolution in aberration-corrected transmission electron microscopes. *Microsc Microanal* **10**(Suppl. 2), 1002–1003.

Peng, Y., Oxley, M.P., Lupini, A.R., Chisholm, M.F. & Pennycook, S.J. (2008). Spatial resolution and information transfer in scanning transmission electron microscopy. *Microsc Microanal* **14**, 36–47.

Pennycook, S.J., Chisholm, M.F., Lupini, A.R., Varela, M., Van Benthem, K., Borisevich, A.Y., Oxley, M.P., Luo, W. & Pantelides, S.T. (2008). Materials applications of aberration-corrected STEM. In *Advances in Imaging and Electron Physics*, Hawkes, P.W. (Ed.), Vol. 153, pp. 1–41. New York: Academic Press.

Rose, H. (1981). Correction of aperture aberrations in magnetic systems with threefold symmetry. *Nucl Instrum Meth* **187**, 187–199.

Rose, H. (1990). Outline of a spherically corrected semiaplanatic medium-voltage transmission electron-microscope. *Optik* **85**, 19–24.

Rose, H. (2003). Advances in electron optics. In *High Resolution Imaging and Spectrometry of Materials*, Ernst, F. & Rühle, M. (Eds.), pp. 189–270. Berlin, New York: Springer.

Scherzer, O. (1936). Über einige Fehler von Elektronenlinsen. *Z Physik* **101**, 593–603.

Scherzer, O. (1947). Sphärische und chromatische Korrektur von Elektronenlinsen. *Optik* **2**, 114–132.

Shao, Z. (1988). On the fifth order aberration in a sextupole corrected probe forming system. *Rev Sci Instrum* **59**, 2429–2437.

Smith, D.J. (2008). Development of aberration-corrected electron microscopy. *Microsc Microanal* **14**, 2–15.

van Benthem, K., Lupini, A.R., Oxley, M.P., Findlay, S.D., Allen, L.J. & Pennycook, S.J. (2006). Three-dimensional ADF imaging of individual atoms by through-focal series scanning transmission electron microscopy. *Ultramicroscopy* **106**, 1062–1068.

Varela, M., Findlay, S.D., Lupini, A.R., Christen, H.M., Borisevich, A.Y., Dellby, N., Krivanek, O.L., Nellist, P.D., Oxley, M.P., Allen, L.J. & Pennycook, S.J. (2004). Spectroscopic imaging of single atoms within a bulk solid. *Phys Rev Lett* **92**, 095502.

Varela, M., Lupini, A.R., van Benthem, K., Borisevich, A.Y., Chisholm, M.F., Shibata, N., Abe, E. & Pennycook, S.J. (2005). Materials characterization in the scanning transmission electron microscope. *Ann Rev Mater Res* **35**, 539–569.

Voyles, P.M., Muller, D.A., Grazul, J., Citrin, P.H. & Gossmann, H.-J. (2002). Atomic-scale imaging of individual dopant atoms and clusters in highly n-type bulk Si. *Nature* **416**, 826–829.

Zach, J. & Haider, M. (1995). Correction of spherical and chromatic aberration in a low-voltage SEM. *Optik* **99**, 112–118.